HAL
open science

High temperature oxidation and embrittlement at 500–600 °C of Ti-6Al-4V alloy fabricated by Laser and Electron Beam Melting

Antoine Casadebaigt, Jonathan Hugues, Daniel Monceau

To cite this version:

Antoine Casadebaigt, Jonathan Hugues, Daniel Monceau. High temperature oxidation and embrittlement at 500–600 °C of Ti-6Al-4V alloy fabricated by Laser and Electron Beam Melting. Corrosion Science, 2020, 175, pp.108875. 10.1016/J.CORSCI.2020.108875 . hal-03033588

HAL Id: hal-03033588

https://hal.science/hal-03033588

Submitted on 1 Dec 2020

HAL is a multi-disciplinary open access archive for the deposit and dissemination of scientific research documents, whether they are published or not. The documents may come from teaching and research institutions in France or abroad, or from public or private research centers.

L'archive ouverte pluridisciplinaire **HAL**, est destinée au dépôt et à la diffusion de documents scientifiques de niveau recherche, publiés ou non, émanant des établissements d'enseignement et de recherche français ou étrangers, des laboratoires publics ou privés.

Open Archive Toulouse Archive Ouverte

OATAO is an open access repository that collects the work of Toulouse researchers and makes it freely available over the web where possible

This is an author's version published in: https://oatao.univ-toulouse.fr/26628

Official URL:

https://doi.org/10.1016/J.CORSCI.2020.108875

To cite this version:

Casadebaigt, Antoine and Hugues, Jonathan and Monceau, Daniel *High temperature oxidation and embrittlement at 500–600 °C of Ti-6Al-4V alloy fabricated by Laser and Electron Beam Melting.* (2020) Corrosion Science, 175. 108875. ISSN 0010-938X.

Any correspondence concerning this service should be sent to the repository administrator: tech-oatao@listes-diff.inp-toulouse.fr

High temperature oxidation and embrittlement at 500–600 °C of Ti-6Al-4V alloy fabricated by Laser and Electron Beam Melting

Antoine Casadebaigt[a,b,*], Jonathan Hugues[a], Daniel Monceau[b]

[a] IRT Saint Exupéry, 3 rue Tarfaya, 31405, Toulouse Cedex 4, France
[b] CIRIMAT, Université de Toulouse, CNRS, INPT, UPS, ENSIACET, 4 allée Emile Monso BP-44362, 31030, Toulouse Cedex 4, France

Keywords:
Titanium
TA6V
Additive manufacturing
SLM
EBM
High temperature oxidation
Oxygen diffusion zone
Oxygen embrittlement

A B S T R A C T

The oxidation kinetics of Ti-6Al-4V alloys fabricated by LBM and EBM, HIP-treated or not, are similar to that of a rolled annealed Ti-6Al-4V alloy, as regards oxide layer and oxygen diffusion layer thickness. Kinetics of oxygen ingress in the metal is independent of the alloy microstructure. At room temperature, the thickness of the brittle layer after a tensile test corresponds to the oxygen diffusion layer, with an oxygen concentration above a critical value that is clearly below 1 at %.

1. Introduction

1.1. Titanium alloys

Titanium alloys are used in aeronautics and in the aerospace industry because of their very high specific mechanical properties and their corrosion resistance at low temperature. Since the 1950s the quantity of titanium alloys in aircrafts has been continuously increasing. Moreover, the operating temperature of engines also increases constantly to improve efficiency and reduce fuel consumption. However, depending on the applications, titanium alloys are limited to temperatures below 600 °C, e.g. 300–400 °C for Ti-6Al-4V (wt.%) [1–4]. This limitation is mainly due to insufficient creep resistance at high temperature [5] and to oxygen embrittlement resulting from the high temperature oxidation. In high temperature environments, titanium alloys form an oxide layer (OL) [6–8]. For Ti, Zr or Hf alloys however, the high solubility of oxygen in the metal induces the formation of an oxygen diffusion zone (ODZ) [9–19], which can be more detrimental than the external oxide scale. This ODZ affects mechanical properties: tensile strength increases while ductility decreases [20–26]. Ti-6Al-4V alloy is one of the oldest titanium alloys, it accounts for nearly 60 % of titanium alloys produced [2] and is frequently used in structural aircraft and jet-engine components [27].

1.2. Additive manufacturing of Ti-6Al-4V

Additive manufacturing (AM) processes are new processes giving the opportunity of a technological leap in the manufacturing of metal parts. In the fields of aeronautics and aerospace, AM processes are a means of reducing part weight and drastically reducing wasted matter, thereby inducing cost savings. Powder bed fusion processes such as Laser Beam Melting (LBM) and Electron Beam Melting (EBM) are processes that have been studied since their development in the 1980s. Both processes use a heating source to selectively melt a powder bed and build the final part layer by layer. LBM uses a laser beam as heating source, whereas EBM uses an electron beam. One of the main differences between the two processes is the pre-heating step of EBM, the powder is maintained at approximately 700 °C to avoid sputtering. Another difference is the atmosphere in the chamber. LBM is done under argon, whereas a vacuum atmosphere is used in EBM [28].

These layer-by-layer processes make it possible to build parts with complex geometry which were impossible to build by using conventional processes such as forging or casting [29]. However, even when parameters are optimized, AM processes may induce defects such as lack of fusion or gas pores. Hot isostatic pressing (HIP) treatment is a heat treatment performed under high pressure, about several hundreds of bars, that enables to reduce residual porosity and improve structural integrity [30].

For the Ti-6Al-4V alloy fabricated by LBM, the high cooling rate

* Corresponding author at: CIRIMAT, Université de Toulouse, CNRS, INPT, UPS, ENSIACET, 4 allée Emile Monso BP-44362, 31030, Toulouse Cedex 4, France.
E-mail addresses: antoine.casadebaigt@hotmail.fr (A. Casadebaigt), daniel.monceau@ensiacet.fr (D. Monceau).

induces a non-equilibrium microstructure. The microstructure of LBM Ti-6Al-4V alloy is entirely composed of acicular martensitic α' phase with prior-β grains elongated in the building direction [31,32]. Due to the pre-heating step of the EBM process, the microstructure of EBM Ti-6Al-4V is composed of thin lamellar α and β phase with prior-β grains elongated in the building direction [33–35]. The HIP treatment of Ti-6Al-4V is usually performed at 920 °C during 2 h at 1000 bars. For EBM Ti-6Al-4V alloy, HIP induces a coarsening of the microstructure, whereas for LBM, it induces the decomposition of the α' martensite into α and β phase [30,36].

1.3. High temperature oxidation of additively manufactured Ti-alloys

As seen above, most literature papers on Ti-6Al-4V alloy fabricated by AM focused on the influence of process parameters on microstructure, defects or mechanical properties. Up to now, only very few studies have focused on the oxidation of titanium alloys fabricated by additive manufacturing. Among them, Karlsson et al., Caballero et al. and Bermingham et al. have studied the oxidation of Ti-6Al-4V alloy during EBM processing and Wire and Arc Additive Manufacturing (WAAM) [37–39]. Three other studies from Terner et al., Som et al. and Wang et al., focused on the oxidation behaviour of titanium aluminides [40–42]. Zhou et al. published the first study on the oxidation of a titanium alloy (Ti-5.5Al-3.4Sn-3.0Zr-0.7Mo-0.3Si-0.4Nb-0.35Ta wt.%) fabricated by LBM [43]. More recently, Liang et al. published a study investigating the oxidation behaviour of Ti-6Al-4V alloy fabricated by Selective Laser Sintering (SLS) [44].

LBM and EBM processes induce a rough surface state presenting partially-melted powder particles. Following the approach developed by Sanviemvongsak et al. [45] for alloy 718, Casadebaigt et al. studied the influence of LBM- and EBM-induced roughness on the oxidation behaviour of Ti-6Al-4V alloy [46]. In this last paper, the effect of sample roughness, but also the effect of the presence of unmelted powder particles at the surface of the samples, were taken into account to quantify oxidation kinetics. This paper showed that oxidation kinetics of additively manufactured samples, compared to manufactured samples, are similar in terms of oxide layer and oxygen diffusion zone thicknesses. It also showed that the higher net mass change per unit area found for additively manufactured samples is due to the combined action of the samples' higher surface area and of fast oxidation kinetics due to the cracking of partially melted powder grains attached to the sample's surface [46].

The present paper follows on from these previous studies and focuses on the influence of the specific surface roughness and microstructure of Ti-6Al-4V titanium alloy, fabricated by LBM and EBM, on its oxidation behaviour. These results are compared to those obtained on a conventionally rolled Ti-6Al-4V alloy. In addition, the influence of HIP treatment on microstructure and oxidation behaviour was studied. The consequences of oxidation on the tensile properties of LBM and EBM Ti-6Al-4V alloys were also assessed.

2. Materials and experimental procedures

2.1. Materials

Ti-6Al-4V alloy samples were fabricated by Laser Beam Melting and Electron Beam Melting. LBM samples were fabricated using an EOS M280 machine equipped with an Yb-fibre laser, at FUSIA, France. Fabrication was made using standard EOS parameters for Ti-6Al-4V alloys to obtain fully dense parts. To limit thermal oxidation, LBM processing was carried out under Ar atmosphere with concentrations below 10 ppm of N_2, 3.0 ppm of O_2 and 1 ppm of H_2O. Plasma atomised Ti-6Al-4V grade 23 powder supplied by AP&C, with a particle size of 15 − 45 μm, was used. The chemical composition of the powder is presented in Table 1. EBM samples were fabricated using an Arcam Q20+ machine equipped with a LaB_6 cathode, at the IRT Saint Exupéry (France) using Arcam parameters and theme 5.2.24. Fabrication was performed under 4.10^{-3} mbar of He. Plasma atomised Ti-6Al-4V grade 23 powder supplied by AP&C with a particle size of 45 − 106 μm was used. The chemical composition of the powder is presented in Table 1. Some samples were submitted to HIP treatment at 920 ± 10 °C and 1020 ± 20 bars for 2 h + 24/−0 min under Ar atmosphere with 1.0 ppm of O_2, 1.5 ppm of N_2 and 4.6 ppm of H_2O at Bodycote, France. Rolled Ti-6Al-4V β-annealed of a 12-mm-thick sheet was used as the conventionally processed Ti-6Al-4V reference. Its chemical composition is presented in Table 1.

2.2. Microstructure and surface characterisations

Five samples of 15 × 10 × 2 mm^3 were used to study the influence of processing and HIP treatment on microstructure. Two samples were fabricated by LBM, one of which was HIP-treated. Two samples were fabricated by EBM, one of which was HIP-treated, and the last sample was rolled β-annealed. The chemical composition of as-built LBM and as-built EBM Ti-6Al-4V alloys are presented in Table 1. The aluminium loss amounts to approximately 1 at.% and almost no change in C, H, O and N concentrations was detected for both LBM and EBM processes. The volatilisation of aluminium is more important for the EBM sample. Juechter et al. studied the evaporation phenomenon during EBM processing of Ti-6Al-4V alloys and showed that aluminium was the most prone to evaporate [47]. Rolled β-annealed samples show a chemical composition that is similar to additively manufactured samples except for oxygen, whose concentration is twice as high.

Microstructure characterisation was performed with a Nikon Eclipse Optical Microscope (OM) after samples were ground with P2400 – SiC abrasive paper, polished with a SiO_2 solution and etched with Kroll reagent for 5 s. Finer observations were obtained using a Scanning Electron Microscopes (SEM) FEI Quanta 450 and LEO 435 VP at 15 kV. The chemical composition was measured with instrumental gas analysis (IGA) and inductively coupled plasma-optical emission spectrometry (ICP-OES) at EAG, France. Phase identification was realised by X-ray diffraction (XRD) at room temperature with a Bruker D8-2 using Cu-Kα radiation in the 2Θ range from 20° to 120° with a step size of 0.02°, a scan step time of 8 s and spinning on samples ground with P1200 – SiC abrasive paper.

In order to study the roughness induced by LBM and EBM processing, as-built samples were characterized and compared to an LBM sample ground with P600 abrasive paper. Roughness was characterized by confocal microscopy. A Zeiss Axio Imager Z2m microscope equipped with a Zeiss LSM800 module was used. For each sample, a square area of 1.6 mm sides was analysed. Results were analysed with ConfoMap ST software, which consisted in removing the abnormal points, filling the holes and adding a 19 × 19 median filter.

2.3. Oxidation experiments

In order to study the influence of surface roughness and alloy microstructure on oxidation behaviour, 39 samples were fabricated by LBM, 39 samples by EBM and one sample was rolled and β-annealed. LBM and EBM samples were 28 × 28 × 2 mm^3 and the rolled β-annealed sample was 15 × 10 × 2 mm^3. Six LBM (As-built LBM) and six EBM (As-built EBM) samples were kept as-built. 19 LBM (LBM P600), 19 EBM (EBM P600) and one rolled β-annealed (rolled P600) samples were ground with P600 – SiC abrasive paper. 14 LBM (LBM HIP P600) and 14 EBM (EBM HIP P600) samples were HIP-treated and ground with P600 – SiC abrasive paper. Grinding was carried out so as to assess the influence of microstructure on oxidation behaviour, independently of the effect of surface roughness of as-built samples. Each sample was cleaned in acetone and then in ethanol in an ultrasonic bath for 1 min prior to oxidation.

Samples were inserted in a pre-heated Carbolite furnace LHT 6/60 with forced convection. An air velocity of about 1 $m{\cdot}s^{-1}$ was measured

Table 1
Chemical composition of Ti-6Al-4V alloys used in this study (measured by Instrumental Gas Analysis (IGA) for O, N, H and C and Inductively Coupled Plasma-Optical Emission Spectrometry (ICP-OES) for Al, V, Fe, Cr and Ti).

	Al (%)	V (%)	Fe (%)	Cr (%)	O (ppm)	N (ppm)	H (ppm)	C (ppm)	Others (%)	Ti
LBM Powder (wt)	6.36	4.03	0.21	0.01	900	100	20	100	< 0.4	Bal
(at)	10.7	3.60	0.17	0.01	2600	300	900	400		Bal
EBM Powder (wt)	6.35	3.68	0.19		800	200	10	100	< 0.4	Bal
(at)	10.7	3.29	0.15		2300	600	500	400		Bal
Rolled β-annealed (wt)	6.41	3.93	0.16		1800	100	40	40	< 0.4	Bal
(at)	10.8	3.51	0.13		5100	300	1800	200		Bal
As-built LBM (wt)	5.99 ± 0.02	4.00 ± 0.02	0.2 ± 0.002	< 0.05	1000	100	30	100		Bal
(at)	10.13	3.58	0.16	< 0.04	2900	300	1400	400		Bal
As-built EBM (wt)	5.59 ± 0.02	4.01 ± 0.01	0.19 ± 0.003	< 0.05	800	140	10	100		Bal
(at)	9.49	3.6	0.16	< 0.04	2300	500	500	400		Bal

in the cold furnace, prior to heating, with a RS-90 Mini Anemometer. For hanging purposes, all samples were drilled with 1.5 mm diameter hole in order to have the highest contact-free area. An opening was present in the top wall of the furnace for atmosphere renewal. Isothermal oxidation treatments were carried out at 500, 538 and 600 °C, for different durations ranging from 25 to 5 000 h. Sample mass were measured before and after oxidation using an electronic balance Sartorius LA 75 3200D with an accuracy of ± 20 µg. Net mass change per unit area (mass gain) values were averaged on three to five measurements for each oxidation test.

2.4. Oxide layer characterisation

The oxide Layer (OL) thickness of samples oxidized at 600 °C was measured using ImageJ. Cross sections, ground with P2400 – SiC abrasive paper and polished with a SiO_2 solution were prepared, and optical microscopies were carried out with a Nikon Eclipse OM. For each sample, 5–10 images were taken and analysed. The image magnification depended on the thickness of the OL. OL thickness was determined by averaging 30–150 measures. For the thinnest OL, cross sections were obtained using a Focused Ion Beam (FIB) at the R. Castaing Microanalysis Centre in Toulouse, France with a SEM/FIB HELIOS 600i. OL thicknesses were determined from SEM images by averaging 10–15 measures.

OL nature was characterized by XRD at room temperature with a Bruker RX D8 GIXRD using Cu-Kα radiation in the 2Θ range from 20° to 80° with a step size of 0.02° and a scan step time of 2 s. In addition, an EDS analysis was performed with a FEI Quanta 450 SEM on the cross section of oxidized samples ground with P2400 – SiC abrasive paper and polished with SiO_2 solution.

2.5. Oxygen diffusion zone characterisation by EPMA

The Oxygen Diffusion Zone (ODZ) was characterized by Electron Probe Microanalyzer (EPMA) at R. Castaing Microanalysis Centre in Toulouse, France, with a CAMECA SX Five FE operating at 15 kV and 20 nA. Oxygen profiles were performed with a machine error of 3 000 wt. ppm on oxygen concentration measurement. For each sample characterized, 3–6 profiles were performed. Due to the presence of a native OL on the surface of the freshly polished cross section, the oxygen signal was biased and had to be corrected. For each profile, three count values were measured in the bulk to determine the count value corresponding to the native OL. The mean count value of the bulk was brought back to zero because the machine error of measured points is six times higher than the oxygen concentration in the bulk. Then, oxygen concentrations in at.% and wt.% were calculated.

2.6. Oxygen diffusion zone characterisation by SIMS

The following samples, all oxidised at 500 °C were analysed by Secondary Ion Mass Spectroscopy (SIMS) : EBM samples oxidised for 100 h and 500 h, and an LBM sample oxidised 500 h. All these samples were ground with P600 SiC paper before oxidation. The depth profiles were obtained through the external oxide scale and in the oxygen diffusion zone below the scale, down through where the oxygen intensity remains constant.

Intensity-depth profiles were measured by SIMS using a Cameca IMS 7f instrument. A Cs + source with a primary current of 40 nA was used in order to reduce the matrix effect. The raster area was 125 × 125 µm^2, and the analysis area 33 × 33 µm^2. The intensities recorded corresponded to the following mass: ^{133}Cs, $^{27}Al^{133}Cs$, $^{48}Ti^{133}Cs$, $^{51}V^{133}Cs$, $^{133}Cs_2$, $^{1}H^{133}Cs_2$, $^{12}C^{133}Cs_2$, $^{14}N^{133}Cs_2$, $^{16}O^{133}Cs_2$. Oxygen concentration profiles were assumed to be given by the following normalisation: the intensity of the signal $^{16}O^{133}Cs_2$ was divided by the average intensity of the same signal found in the core of the sample and multiplied by the oxygen concentration in the core of the sample. The oxygen concentration in the core of the sample was measured by IGA and is given in Table 1. This normalisation procedure led to an oxygen concentration below the oxide scales lying between 20 at.% and 30 at.%. The position of the metal/oxide interface was chosen close to the inflexion point of the oxygen concentration profile, where the concentration was close to 25 at.% which was consistent with EPMA measurements.

All sputtering craters were analysed by contact profilometry with a Bruker Dektak 8 instrument. This measurement was used to calculate the depth of the SIMS analysis from the duration of the sputtering. Average crater depth was about 10 µm with a roughness of about +/-0.5 µm at the bottom of the crater. The average oxide thickness was about 70 nm. Depth measurement uncertainty leads to a 15 % error on the determination of D.

2.7. Tensile tests

Tensile tests were performed on a MTS2 Criterion at MIDIVAL using a high temperature Epsilon extensometer of 20 mm working distance to measure displacement. Tensile specimens had a gauge area of 30 × 5 mm^2, a thickness of 1.3 mm and were ground with P600 – SiC abrasive paper. In order to investigate the influence of oxidation on tensile properties, samples were pre-oxidized at 600 °C during 500 h in the Carbolite furnace LHT6/60 before running tensile tests. Rupture surfaces were observed using LEO 435 VP SEM. ODZ thickness was determined by measuring the distance between two points in order to draw a line perpendicularly to the metal/oxide interface. For both oxidized samples, the average value of ODZ thickness was obtained from 40 to 80 measures.

3. Results

3.1. Microstructures

Fig. 1 shows the microstructure of Ti-6Al-4V titanium alloys in five metallurgical states observed using OM and SEM. The rolled β-annealed

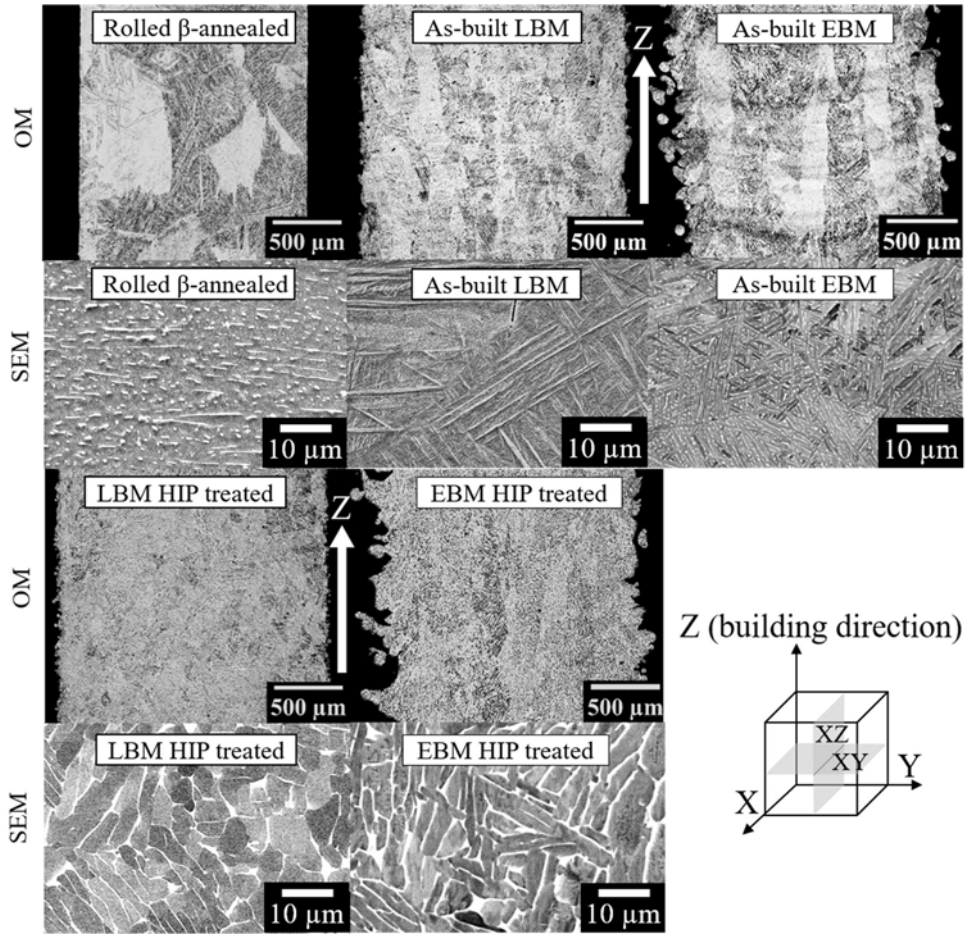

Fig. 1. Optical (OM) and Scanning Electron microscopies (SEM) of rolled, LBM and EBM Ti-6Al-4V alloys.

Table 2
Thicknesses of α-laths of rolled, LBM and EBM Ti-6Al-4V alloys.

	Rolled β-annealed	As-built LBM (α' laths)	As-built EBM	LBM HIP treated	EBM HIP treated
α-laths thickness (µm)	1.0 ± 0.3	< 0.9	0.7 ± 0.2	2.1 ± 0.7	2.5 ± 0.4

sample presents large prior-β grains without any preferential grain orientation, whereas as-built LBM and as-built EBM samples both have prior-β grains elongated along the building direction. HIP treatment partly "erases" prior-β grains in HIP-treated LBM samples whereas in HIP-treated EBM samples, the solidification structure is still clearly visible. SEM observations reveal that rolled β-annealed microstructure is composed of α and β phase, similarly to as-built EBM microstructure but with α-laths being about 1 µm thick, as shown in Table 2. As-built LBM microstructure is composed of fully acicular martensitic α'-laths, with a maximum thickness of 0.9 µm, as reported in Table 2. HIP treatment on as-built LBM samples induced the transformation of α'-laths into α and β phase. In addition, HIP treatment induced a large coarsening of α-laths in both as-built LBM and as-built EBM samples, as presented in Table 2. After the HIP treatment, the microstructures of LBM and EBM samples are similar.

Fig. 2 shows the X-ray diffractograms obtained for the different Ti-6Al-4V alloys, i.e. rolled β-annealed, as-built LBM, as-built EBM, HIP-treated LBM and HIP-treated EBM. XRD of as-built LBM indicates the presence of an hexagonal phase only, corresponding to α' martensite. XRD analyses of as-built EBM and HIP-treated LBM/EBM samples show peaks corresponding to both α and β phases. In the XRD diffractogram of rolled β-annealed the α peaks appear clearly but the main peak corresponding to the (1 1 0) planes of the β phase of Ti-6Al-4V at 39.5°

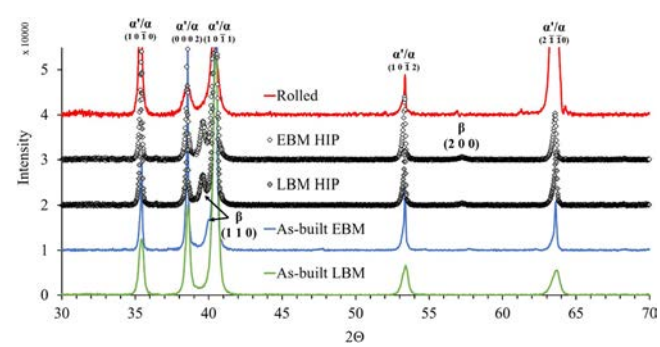

Fig. 2. Comparison of X-ray diffractions of unoxidized Ti-6Al-4V alloys (intensities are normalised by their highest value for each diagram).

does not appear. However, a small peak corresponding to the (2 0 0) planes of the β phase appears at 57°. The intensity of β peaks is rather low because the volume fraction of β phase is small. In addition, in the diffractogram of the as-built EBM sample, the (1 1 0)– β peak around 39.5° is not well separated from the (1 0 $\bar{1}$ 1)– α peak around 40.5°. Table 3 presents the lattice parameters of each sample estimated from XRD. All five samples have similar α-phase lattice parameters. The β-

Table 3
Lattice parameters of Ti-6Al-4V alloys estimated from X-ray diffractions.

		Rolled β-annealed	As-built LBM (α')	As-built EBM	LBM HIP treated	EBM HIP treated
Ti-α	*a* (Å)	2.93	2.92	2.92	2.92	2.93
	c (Å)	4.67	4.66	4.67	4.67	4.68
Ti-β	a (Å)	3.22		3.19	3.21	3.22

phase lattice parameter however, is lower in EBM than in rolled and HIP-treated EBM/LBM samples.

As seen in a previous study [46], Ti-6Al-4V alloy fabricated by LBM has a rough surface that can be described as a wavy surface with the presence of partially melted powder grains. Fig. 3 shows the surface of as-built LBM and as-built EBM samples. Here too, both types of samples exhibit a wavy surface with the presence of partially melted powder grains over it. At this point, it should be reminded that the powder grains used in the EBM process are larger than those used in LBM, resulting in larger powder grains on the surface. Fig. 4 shows the 3D surface reconstruction from confocal microscopy of an LBM sample ground with P600 – SiC abrasive paper (LBM P600), of an as-built LBM sample and of two areas of an as-built EBM sample. Area 1 from as-built EBM samples corresponds to the bottom of the sample and Area 2 corresponds to the top of the sample. In order to compare the surface roughness of these samples, the notions of projected surface area, S_{par}, and developed surface area, S_{dar}, are used. S_{dar} corresponds to the area of the developed surface which takes surface topography into account. Therefore, the ratio $\frac{S_{dar}}{S_{par}}$ gives the evolution in surface area induced by surface roughness. For LBM P600 the ratio is close to 1, whereas for as-built LBM the ratio is 2.1, and for as-built EBM it varies between 2.2 and 4.6. These values show that there is a variation in surface roughness along the height of as-built EBM sample. Such discrepancies were not observed on as-built LBM samples.

3.2. Oxidation kinetics

Fig. 5 presents the net mass change per unit area, expressed in $mg{\cdot}cm^{-2}$, of samples oxidized at 500, 538 and 600 °C as a function of the square root of time. Error bars were calculated from errors made on surface area from calliper measurements and on mass gain from the electronic balance. Samples that were oxidized for 1000 h at 600 °C and rolled P600 oxidized for 500 h at 600 °C spalled during cooling. When spallation occurred, mass gain values are slightly underestimated, therefore these points were not considered for the oxidation kinetics quantification. Whichever the temperature, as-built LBM and EBM samples have a higher mass gain than LBM P600 and EBM P600 ground samples. Ratios between the mass gain per unit area of as-built and ground samples for LBM and EBM was calculated by dividing net mass change per unit area (measured with a calliper as the projected area) of as-built sample by net mass change per unit area of ground sample. These ratios vary from 2.5 to 6 for LBM and EBM samples. At all investigated temperatures, ground samples exhibit similar mass gain, i.e. LBM P600, EBM P600, LBM HIP P600 and EBM HIP P600 samples; except at 600 °C, where the LBM P600 sample shows slightly lower oxidation kinetics. Fig. 6 is an Arrhenius plot comparing the oxidation kinetics obtained from this study with the literature data, as explained in a previous paper [46]. All literature-based results were recalculated from initial literature net mass change per unit area data using the simple parabolic law $\frac{\Delta m}{A} = \sqrt{k_p{\cdot}t}$ where Δm is the net mass change (mg), A the area of the sample (cm^2), k_p the parabolic rate constant and t the time. Literature data that were too far from a simple parabolic law were not used in this Arrhenius plot. This was the case for literature data obtained at temperatures above 800 °C, for which the oxidation kinetics become often linear after the initial parabolic regime. In the present study, a kinetic transition was observed at approximately 200 h at 538 °C and 600 °C in as-built LBM and EBM samples (Fig. 5). Because of this, it was not possible to determine a single parabolic constant. Based on a previous study [46], it was concluded that this change of behaviour was due to the combined effects of the parabolic oxidation of the surface and the non-parabolic oxidation of the partially-melted powder grains, which cracked during oxidation [46]. Fig. 6 shows that the present results are in good agreement with the literature. At 600 °C, the oxidation kinetics of LBM and EBM samples is similar to that of rolled samples.

Fig. 7 displays the oxide layer (OL) thicknesses of samples oxidized at 600 °C. The plot shows that oxide scale growth follows a parabolic kinetics until the oxide scale thicknesses reaches 6 – 10 μm. OL thicknesses of as-built LBM and as-built EBM samples seems to be 1.4 times larger than those of LBM P600 and EBM P600 samples. Nevertheless, it can be noticed that the standard deviation is relatively high, and these differences of 40 % lie in the domain covered by the error bars. Similarly to what was found for mass gain, ground samples have similar OL thicknesses except for the LBM P600 sample.

Fig. 8 shows the cross sections of the as-built and ground LBM and EBM samples oxidized in different conditions. Fig. 8 a) and b) show that OL of as-built samples oxidized 500 h at 600 °C, well follow the highly wavy surfaces. It can be seen that is it easy to overestimate the OL thickness because the oxide can be seen under the plane of the cross section. This has induced the high standard deviation for as-built OL thicknesses, presented in Fig. 7. At this stage of oxidation, it can be seen also that the oxide layer around one alloy particle lying at the surface, has the same thickness as the rest of the sample. The oxide layers obtained after 500 h at 500 °C on ground LBM and EBM samples (Fig. 8c and d) are thinner than after 500 h at 538 °C (Fig. 8e and f), which are themselves, thinner than after 500 h at 600 °C (Fig. 8g and h). This shows the high dependence of OL thickness with the temperature. Fig. 8 c) to h) show the presence of pores inside the OL and it can be seen that the quantity of pores inside the OL increase with the temperature for both LBM and EBM samples. The oxide layers of LBM and EBM samples obtained at 600 °C present the same morphology: a middle layer with a low amount of pores surrounded by an inner and an outer layer with a high amount of pores. In addition, a high amount of pores at the metal/

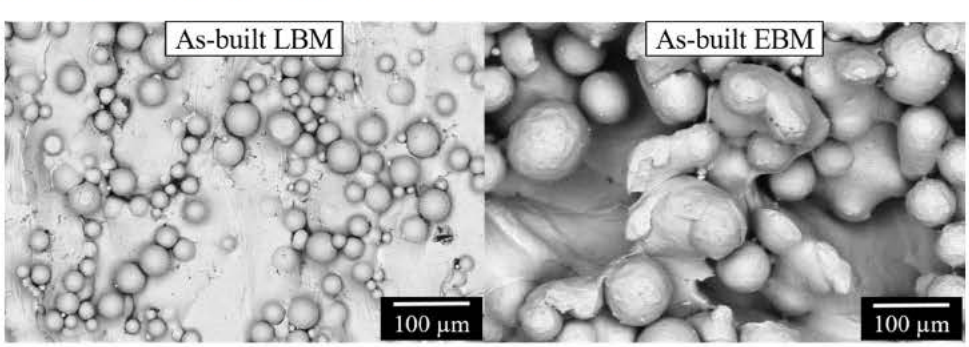

Fig. 3. Surface state of as-built LBM and as-built EBM samples.

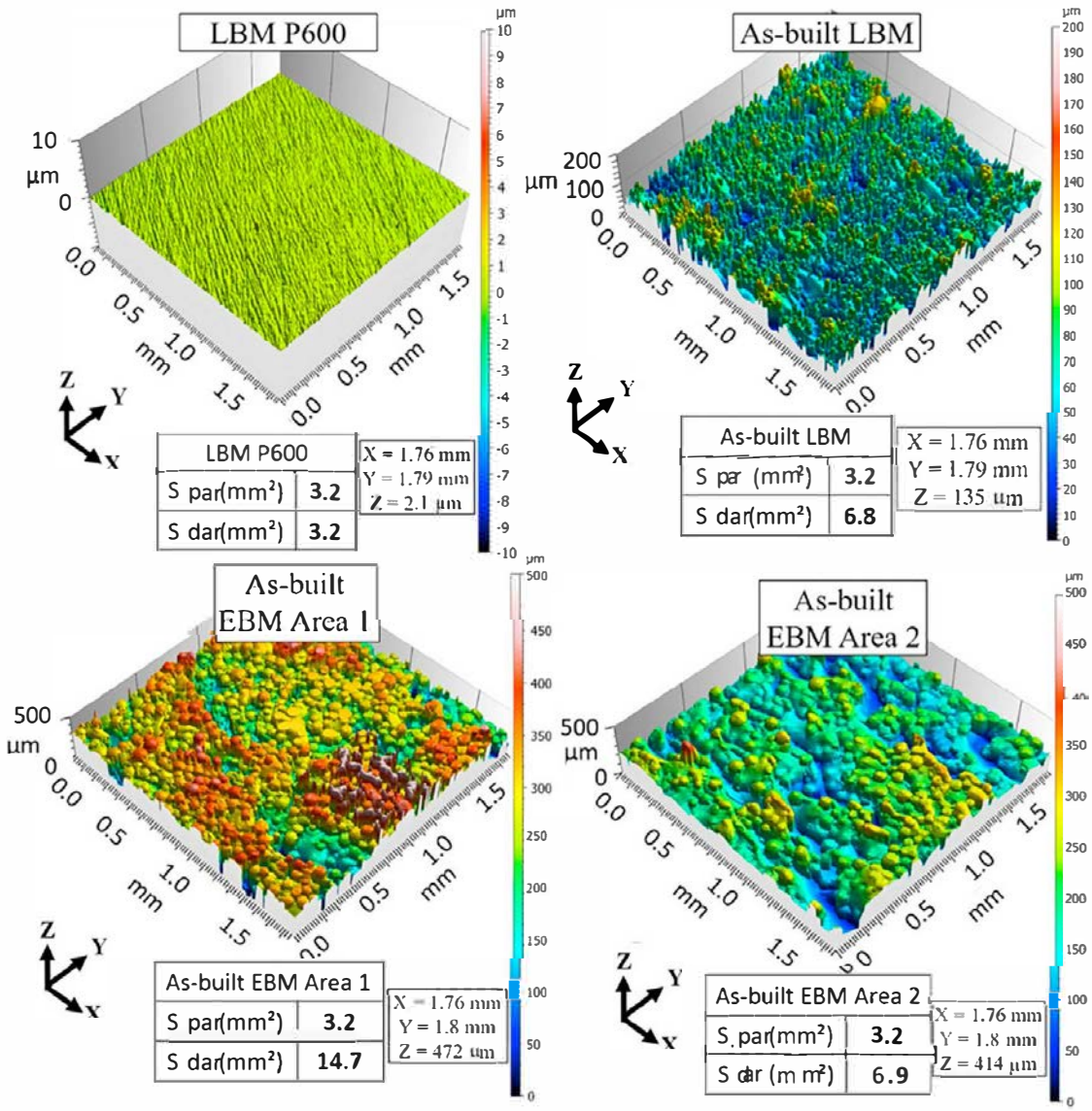

	Sdar/Spar ratio
LBM P600	1.0
As-built LBM	2.1
As-built EBM Area 1	4.6
As-built EBM Area 2	2.2

Fig. 4. Characterisation of surface roughness by confocal microscopy of Ti-6Al-4V alloys before and after grinding.

oxide interface is observed in the four samples oxidized 500 h at 538 °C and 600 °C. Lastly, small white precipitates (SEM in BSE mode) can be seen in Fig. 8, they correspond to the β phase. Fig. 9 a) presents OL diffractograms of LBM P600 and EBM P600 oxidized 500 h at 600 °C. Both results show the presence of rutile TiO_2 in the OL. Fig. 9 b) displays EDS cartographies of the OL on LBM P600 and EBM P600 samples oxidized 500 h at 600 °C. EDS cartographies show the presence of outer aluminum-rich layers in both oxide layers. Several authors found that the oxide scales forming on Ti-6Al-4V alloy were stratified with several rutile and alumina layers. This same structure was observed in this study on LBM and EBM processed samples [8,48–51].

3.3. Oxygen diffusion zone and O diffusion coefficient

Fig. 10 shows an example of experimental EPMA profile obtained from an LBM P600 sample oxidized 500 h at 600 °C. To determine the effective diffusion coefficient of oxygen (D) in the metal, experimental EPMA profiles were fitted using the solution of the second Fick law, Eq. (1), with the oxygen concentration at the metal/oxide interface, Cs, and D being constant. To determine the ODZ, the criteria $ODZ = 4 \cdot \sqrt{D \cdot t}$ was chosen, based on the ratio $\frac{(C_x - C_0)}{(C_s - C_0)} = 0.005$, presented in Eq. (2). This corresponds to the metal thickness value for which an oxygen concentration is about 0.5 at.% for most samples. This criteria has the advantage of being independent of the operator.

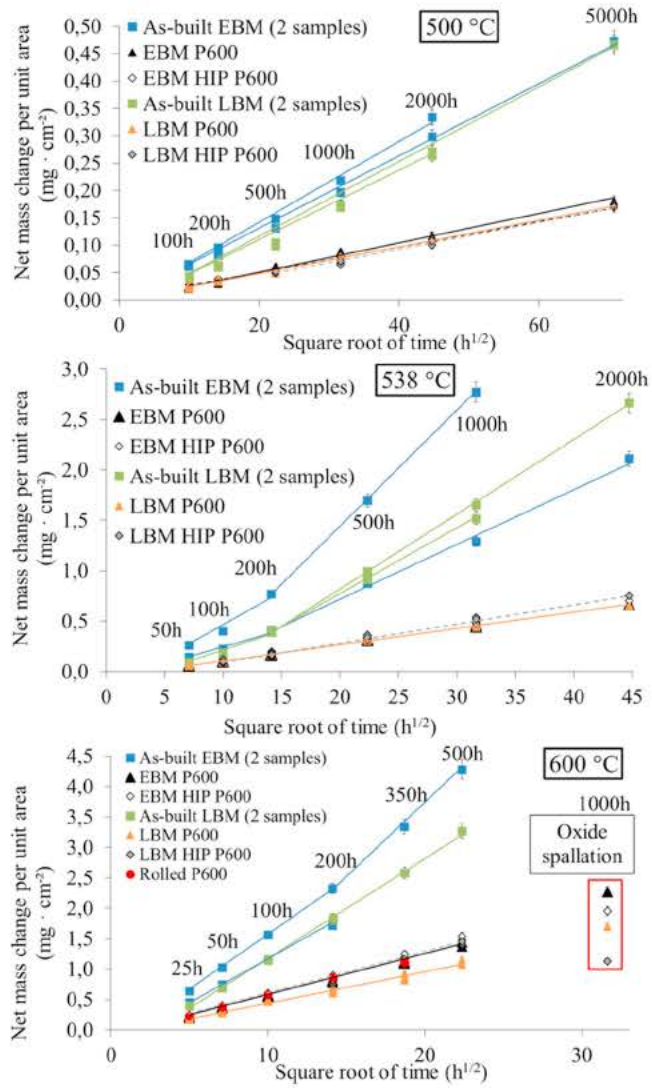

Fig. 5. Net mass change per unit area kinetics of Ti-6Al-4V alloys oxidized at 500, 538 and 600 °C.

$$C_x = C_0 + (C_S - C_0)\cdot\left(1 - erf\left(\frac{x}{2\sqrt{D\cdot t}}\right)\right) \quad (1)$$

$$\frac{(C_x - C_0)}{(C_s - C_0)} = 1 - erf(2) \approx 0.005 \quad (2)$$

Fig. 11 presents fitted EPMA profiles of LBM and EBM samples oxidized for 500 h at 600 °C and 2000 h at 500 °C. Table 4 shows the values of D and ODZ thicknesses found in this study. Despite large differences in microstructure and surface roughness, it is remarkable that after 500 h of oxidation at 600 °C all samples have the same ODZ. The same remark can be made for samples oxidized 2000 h at 500 °C. The diffusion coefficients of oxygen found in this study are compared to literature data in an Arrhenius plot in Fig. 12. This plot presents oxygen diffusion coefficients determined by fitting microhardness profiles by Vaché et al. [52] on conventionally processed Ti-6Al-4V alloys, oxygen diffusion coefficients determined by fitting microhardness profiles from the literature using Vaché et al.'s model, oxygen diffusion coefficients determined by SIMS from Poquillon et al. and oxygen diffusion coefficients D obtained in the present study by fitting EPMA and SIMS profiles. As for EPMA profiles, SIMS profiles were fitted using the solution of the second Fick law, Eq. (1), with Cs fixed between 20 at.% and 30 at.% and D being constant, Table 5. Diffusion coefficients of oxygen are in good agreement with literature data and show that microstructure only

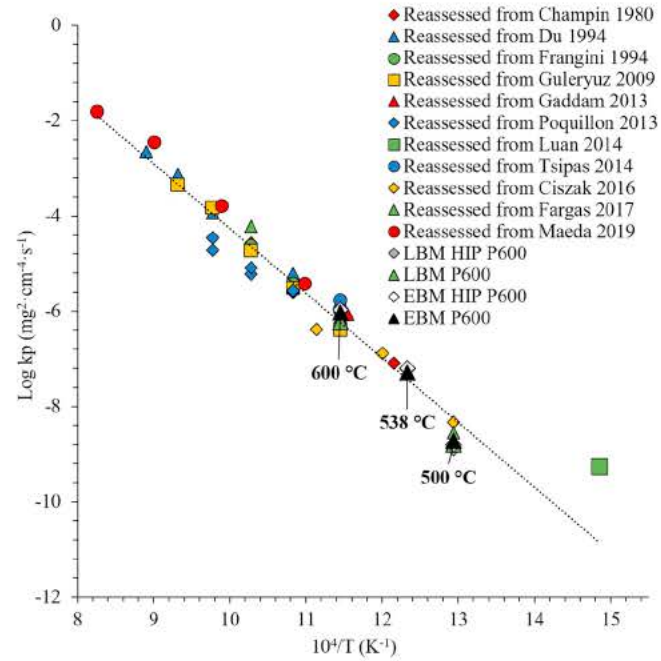

Fig. 6. Arrhenius plot of oxidation parabolic constants measured for Ti-6Al-4V alloys of this study compared with reassessed literature data [7,8,13,15,19,71–76].

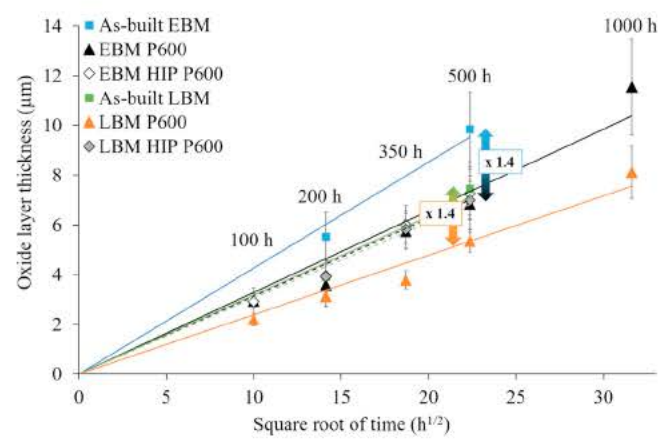

Fig. 7. Oxide layer thicknesses of Ti-6Al-4V alloys oxidized at 600 °C.

has a small influence on the diffusion of oxygen in the metal. Calculations leads to a pre-exponential factor $D_0 = 4.0\cdot10^{-4}\,m^2\cdot s^{-1}$ and an activation energy of $Q = 219\,kJ\cdot mol^{-1}$. These values are close to those obtained by Liu et al. in α-titanium, indicated by the red line in Fig. 12 [53].

3.4. Embrittlement

Fig. 13 presents the rupture surfaces of a) LBM P600 and ; b) and c) EBM P600, both oxidized 500 h at 600 °C, after tensile tests performed at room temperature. The OL spalled during tensile tests and are not present on the rupture surface. The following observations can be made: presence of two different rupture modes; presence of a ductile zone with dimples in the bulk of the specimen; and presence of a brittle zone near the surface. An area of high plastic strain is present between the ductile and the brittle areas and appears as a crest in Fig. 13. The rupture mode changes as O enrichment increases, from a ductile rupture to a brittle rupture [23,24,54]. The brittle zone is the closest to the surface and the most oxygen-enriched. The high plastic strain area corresponds to the specimen's last section of mater before rupture

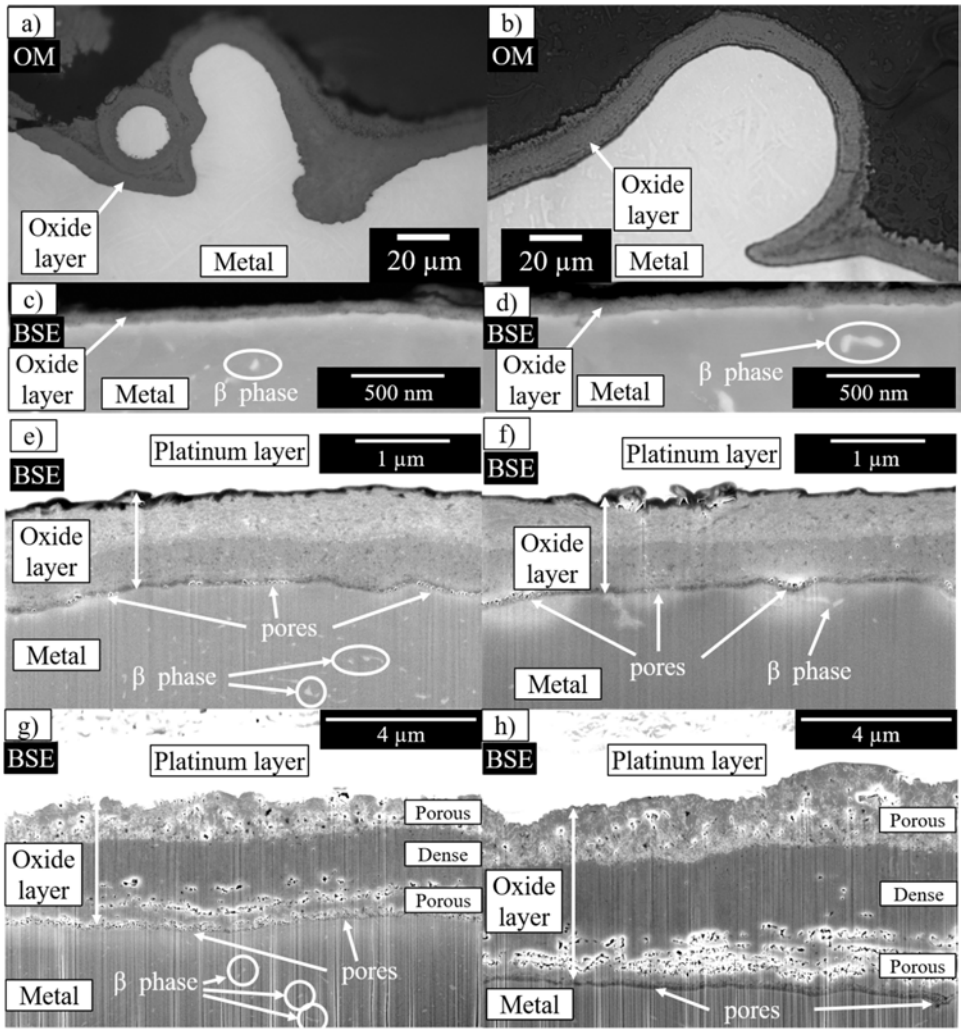

Fig. 8. Optical microscopies of a) as-built LBM oxidized 500 h at 600 °C, b) as-built EBM oxidized 500 h at 600 °C. SEM observations in BSE mode of FIB cross sections of c) LBM P600 oxidized 500 h at 500 °C, d) EBM P600 oxidized 500 h at 500 °C, e) LBM P600 oxidized 500 h at 538 °C, f) EBM P600 oxidized 500 h at 538 °C, g) LBM P600 oxidized 500 h at 600 °C and h) EBM P600 oxidized 500 h at 600 °C.

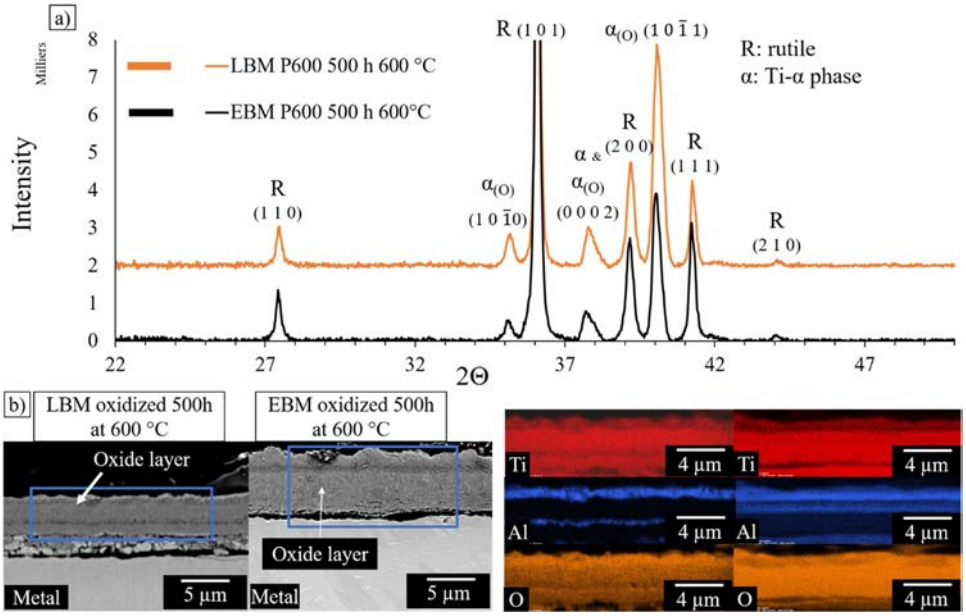

Fig. 9. a) X-ray diffraction and b) EDS of LBM and EBM Ti-6Al-4V alloys oxidized 500 h 600 °C.

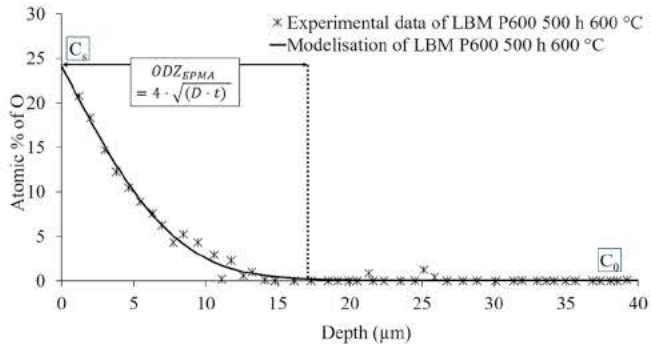

Fig. 10. Fitting of EPMA profiles and determination of ODZ thickness with $ODZ = 4 \cdot \sqrt{D \cdot t}$.

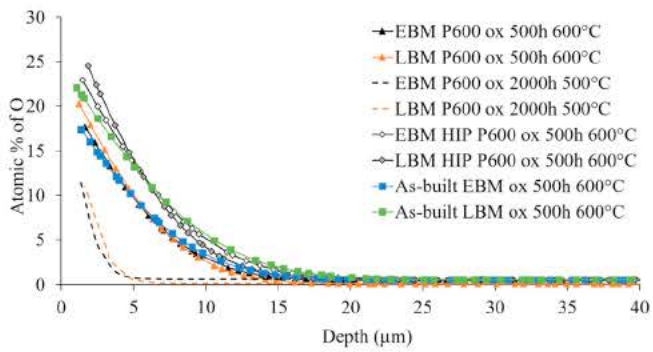

Fig. 11. Fitted EPMA oxygen concentration profiles, using Eq. (1), of LBM and EBM samples oxidized 500 h at 600 °C and 2000 h at 500 °C.

occurs. For 500 h at 600 °C, the brittle zone affected by oxygen is about 25 µm deep for both LBM and EBM samples.

4. Discussion

The microstructure of Ti-6Al-4V strongly depends on the manufacturing process and the heat treatments. As-built EBM and rolled β-annealed samples have thin lamellar microstructures. HIP-treated LBM and EBM samples both have a coarser (α + β) lamellar microstructure. Fig. 1 shows the very thin, needle-like microstructure of as-built LBM and XRD in Fig. 2 only shows peaks from an hexagonal crystallographic structure. This could be an acicular α' microstructure. However, when lattice parameters of the hexagonal α phase reported in Table 3 are compared, there is no clear difference between those from α and α' phases. No shift of α peaks was observed, contrary to what is stated in the literature [36,55]. Wide and asymmetric XRD peaks from the α'-phase of the as-built LBM alloy could be due to the presence of residual stresses induced by the local high cooling rate during manufacturing, otherwise it could be due to the extremely thin α'-laths [56–62]. Fig. 2 also shows that the (1 1 0) β-peak of the as-built EBM sample, which should be around 39.5°, appears at a higher angle and is overlapped by the $(1\,0\,\bar{1}\,1)$-α peak. In the XRD of rolled β-annealed the (1 1 0)-β peak does not appear, but the (2 0 0)-β peak is slightly visible. The (1 1 0)-β peak might be included into the $(1\,0\,\bar{1}\,1)$-α peak

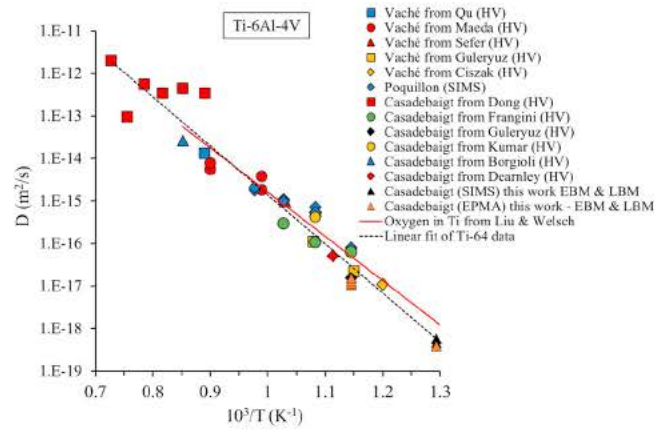

Fig. 12. Arrhenius plot of the effective oxygen diffusion coefficients in Ti-6Al-4V obtained by: fitting microhardness profiles from literature by Vaché et al. [52] and by the authors [13,51,77–80] using the model developed by Vaché et al., diffusion coefficients of oxygen measured by SIMS from Poquillon et al. [72], and by fitting EPMA and SIMS concentration profiles in the present study. For comparison, oxygen diffusion coefficients in alpha-titanium from Liu and Welsch [53].

The first aim of the study was to characterize the oxidation kinetics of additively manufactured (AM) Ti-6Al-4V and to compare it with the oxidation kinetics of the conventionally processed alloy. AM alloys may behave differently because of their specific microstructure, their possible chemical and structural inhomogeneities, their defects or their rough surfaces.

4.1. Effect of surface morphology on oxidation kinetics

First, surface morphology will be discussed. In powder bed additive manufacturing processes, partially-melted powder particles can be found on the surface of the samples, as depicted in Fig. 3. Confocal microscopy revealed that roughness of as-built LBM and EBM samples is high compared to a sample ground with P600 – SiC abrasive paper. In order to calculate the net mass change per unit area, the surface area should be thoroughly studied. Oxidation experiments are usually performed on ground samples so that the effect of roughness can be neglected. In this study, some LBM and EBM samples were kept with as-built surfaces and submitted to oxidation treatments. Fig. 4 presents the characterisation of the surface areas of a ground sample and as-built samples. Results from the LBM ground P600 show that surface roughness is negligible because it is much smaller than the oxide layer thicknesses. However, results also indicate that the developed surface of as-built LBM and EBM samples is 2–5 times higher than for a ground surface. Net mass change per unit area presented in Fig. 5 are calculated with the projected flat surface area. These show that mass gain of as-built LBM and EBM samples are higher than mass gain of ground LBM and EBM samples. Fig. 7 and Table 4 show that as-built LBM/EBM samples could have slightly larger OL thicknesses and ODZ thicknesses than for ground samples. By gathering the results regarding developed surface area, net mass change per unit area, OL and ODZ thicknesses, it can be concluded that surface roughness does not influence much the

Table 4
Effective diffusion coefficients of oxygen in the metal, D, calculated from EPMA O concentration profiles, and ODZ thicknesses.

Oxidation conditions	Oxidized 2000 h at 500 °C	Oxidized 2000 h at 500 °C	Oxidized 500 h at 600 °C	Oxidized 500 h at 600 °C	Oxidized 500 h at 600 °C	Oxidized 500 h at 600 °C	Oxidized 500 h at 600 °C	Oxidized 500 h at 600 °C
Samples	EBM P600	LBM P600	EBM P600	LBM P600	EBM HIP P600	LBM HIP P600	As-built EBM	As-built LBM
D (10^{-19}) ($m^2 \cdot s^{-1}$)	3.9 ± 1.5	3.9 ± 0.7	106 ± 19	117 ± 17	160 ± 27	117 ± 31	133 ± 15	154 ± 70
ODZ (µm)	6 ± 1	7 ± 1	17 ± 2	18 ± 1	21 ± 2	18 ± 2	20 ± 1	21 ± 5
Cs (at.%)	22 ± 3	25 ± 5	23 ± 2	25 ± 1	26 ± 4	30 ± 2	23 ± 3	28 ± 2

Table 5
Effective diffusion coefficients of oxygen in the metal measured by SIMS.

	EBM P600 500 h at 500 °C Profile 1	EBM P600 500 h at 500 °C Profile 2	EBM P600 100 h at 500 °C	LBM P600 500 h at 500 °C
Cs (at.%)	24.7	25.2	23.5	25.6
D (m^2/s)	$4.6 \pm 0.3 \times 10^{-19}$	$5.6 \pm 0.6 \times 10^{-19}$	$5.9 \pm 0.9 \times 10^{-19}$	$5.8 \pm 0.9 \times 10^{-19}$

formation of the OL and the ODZ. Surface roughness effect is small in terms of sample thickness affected by oxidation. The higher mass gain found in as-built samples can be explained by the fact that their developed surface area is more important.

However, due to the surface morphology of as-built LBM and EBM samples, the measuring of the developed surface area by confocal microscopy leads to some errors. One of these errors relies on the fact that confocal microscopy uses 2D imaging and focus determination to reconstruct a 3D surface. As a consequence, some parts of the surface are hidden, as in the case of partially-melted powder particles. Fig. 14 shows the error made when measuring the S_{dar} of a partially-melted powder grain on a planar surface, calculated with Eq. (3). Two extreme situations were considered: a powder particle having only one single contact point with the surface and a powder particle half-melted onto the surface. The maximum error – approximately 20 % – corresponds to the single contact point situation. However, this situation rarely appears on as-built Ti-6Al-4V samples. Moreover, LBM and EBM samples are not entirely covered with partially-melted powder particles. Therefore, the error made on the S_{dar} determination by confocal microscopy should be much lower than 20 %.

$$\frac{\textit{Developped surface}}{\textit{Measured surface with confocal}} = \frac{(5 \cdot R^2 - 4 \cdot R \cdot h + h^2)}{(4 \cdot R^2 - 2 \cdot R \cdot h)} \quad (3)$$

4.2. Effect of microstructure on oxidation kinetics

The influence of microstructure on oxidation kinetics is shown in Fig. 5. As presented above, the samples were ground with P600 – SiC abrasive paper in order to neglect the influence of surface topography. At all the temperatures of interest, mass gain are similar for all the ground samples – LBM P600, EBM P600, HIP-treated LBM and EBM P600, and rolled P600 – despite their large microstructural differences. The only exception is the LBM P600 sample oxidized at 600 °C. Table 6 summarizes net mass change per unit area, OL and ODZ thicknesses for LBM & EBM P600 and LBM & EBM HIP P600 samples oxidized for 500 h at 600 °C and 2000 h at 500 °C. It can be seen that the lower mass gain of the LBM P600 comes from its smaller OL thickness. The first question consisted in finding whether this smaller OL thickness resulted from the metastable α' microstructure inherited from LBM. In Fig. 8 c), e) and g) however, the presence of a lighter phase, the β phase, demonstrates that the microstructure of LBM samples evolves during the oxidation treatment. In Fig. 15 the peak of the (2 0 0) planes of the β phase is present at about 57°; this confirms that the transformation of the α' martensitic microstructure into a (α + β) microstructure occurred in all samples

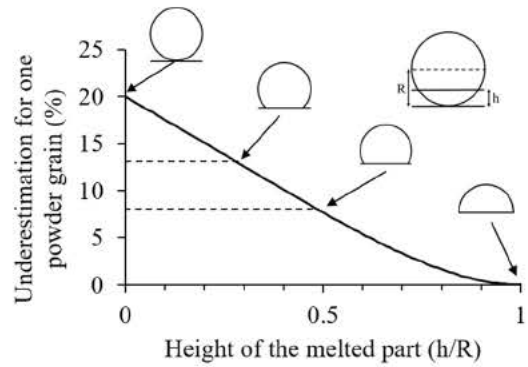

Fig. 14. Underestimation of developed surface (S_{dar}) determined by confocal microscopy.

except for the one that was oxidized 500 h at 500 °C. The volume fraction of β is too small to be detected. The two samples oxidized at 538 and 600 °C have their main (1 1 0)-β phase peak clearly distinct from their (1 0 $\bar{1}$ 1)-α phase peak, this is not the case for the sample oxidized 5000 h at 500 °C. Fig. 15 shows that after 500 h at 600 °C α' completely transformed into α + β, as no difference is observed with the diffractogram obtained after 1000 h at 600 °C. Whereas after 500 h at 538 °C, the transformation is not complete yet because β peaks are still shifting up to 2000 h. The shift in diffraction angle of the (2 0 0)-β peak could be explained by the chemical composition of the β phase which is different depending on the progress of the phase transformation and the temperature. For Ti-β phase the shift in diffraction angle of β peaks could be due to the concentration of vanadium in the β phase. Calculations of V and Al content in α and β phases, performed with Thermo-Calc software using the TCTI 1 database, are presented in Fig. 16. These results are in good agreement with Elmer et al. who calculated the same element contents with Thermo-Calc using the Ti-data database [63]. These calculations show that the partitioning of vanadium increased as temperature decreased. In the β phase, the higher the vanadium concentration, the smaller the lattice parameters, because the atomic size of vanadium is smaller than titanium's [64]. These smaller lattice parameter shift the diffraction angles towards higher values [63]. This study demonstrated that a heat treatment performed for 500 h at 538 and 600 °C induces the transformation of the α' martensitic phase into a α + β microstructure. Since the oxidation treatment was not performed on α' martensite only, the oxidation kinetics of α' martensite was not characterized. From these results, it was not possible to determine whether the lower OL thickness of the

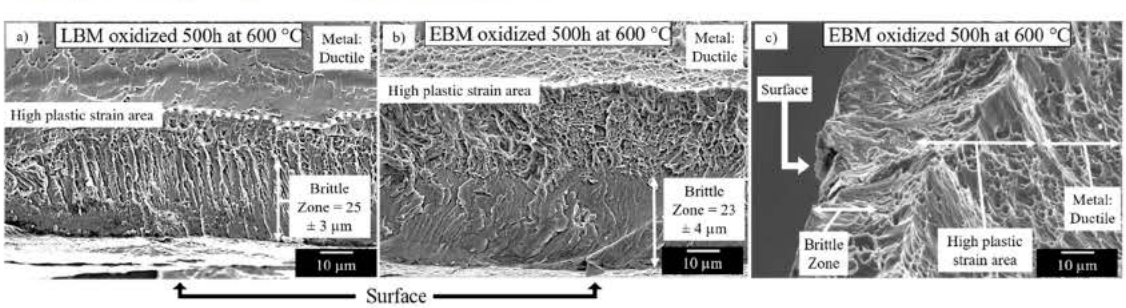

Fig. 13. Rupture surface of LBM and EBM tensile specimens oxidized 500 h at 600 °C.

Table 6
Net mass change per unit area proportion due to oxide layer (OL) growth and due to dissolved oxygen in the metal (ODZ). (* calculated from OL thickness measurements; ** calculated from EPMA measurements).

	LBM P600 500 h 600 °C	EBM P600 500 h 600 °C	LBM HIP P600 500 h 600 °C	EBM HIP P600 500 h 600 °C	LBM P600 2000 h 500 °C	EBM P600 2000 h 500 °C
ODZ thickness (μm)	18 ± 1	17 ± 2	18 ± 2	21 ± 2	7 ± 1	6 ± 1
OL thickness (μm)	5.4 ± 0.5	6.8 ± 1.1	7.0 ± 0.8	7.3 ± 1.0	0.14 ± 0.01	0.14 ± 0.01
$\frac{\text{ODZ thickness (μm)}}{\text{OL thickness (μm)}}$	≈ 3.3	≈ 2.5	≈ 2.6	≈ 2.9	≈ 50	≈ 43
OL net mass change per unit area (mg·cm^{-2})	0.91 ± 0.1	1.16 ± 0.2	1.19 ± 0.1	1.23 ± 0.2	0.02 ± 0.00	0.02 ± 0.00
ODZ net mass change per unit area (mg·cm^{-2})	0.24 ± 0.02	0.22 ± 0.03	0.29 ± 0.04	0.27 ± 0.03	0.11 ± 0.02	0.12 ± 0.02
Total net mass change per unit area (mg·cm^{-2})	1.07 ± 0.04	1.38 ± 0.06	1.41 ± 0.05	1.48 ± 0.06	0.11 ± 0.01	0.12 ± 0.01
% of net mass change per unit area due to ODZ	* 15 ± 7	* 16 ± 14	* 16 ± 9	* 17 ± 12	* 78 ± 2	* 80 ± 1
	** 22 ± 2	** 16 ± 2	** 21 ± 3	** 19 ± 2	** 103 ± 18	** 88 ± 17

LBM P600 oxidized at 600 °C was due to its metastable microstructure. LBM HIP P600 and EBM HIP samples have similar microstructures. Despite differences in chemical composition they present similar oxidation kinetics. The influence of slight variations in chemical composition on oxidation kinetics is therefore excluded.

EBM P600 and EBM HIP P600 results summarized in Table 6 show that despite the fact that the HIP-treated sample has a microstructure twice as coarse and a lower density of α-lath interfaces, oxidation kinetics as well as OL and ODZ thicknesses are similar. These results confirmed that the diffusion of oxygen in Ti-6Al-4V is not controlled by the diffusion of oxygen at the α-lath interfaces, contrary to what Sugahara et al. explained in a previous study [65]. This finding is also in contradiction with Leyens et al. and Sai Srinadh et al. who found that the oxidation kinetics of IMI 834 and TIMETAL 1100 changed depending on microstructure [66,67].

4.3. New data for low temperature oxidation kinetics and oxygen diffusion

Fig. 6 shows that at 600 °C, the oxidation kinetics of additively manufactured LBM and EBM samples is similar to that of the rolled β annealed Ti-6Al-4V alloy used in this study, and also to that of the different conventionally processed Ti-6Al-4V alloys from the literature. Very few literature data exist regarding temperatures below 600 °C. At 500 °C, we found that oxidation kinetics are slightly lower than the extrapolation from high temperature literature data. This can be explained by the formation of a less-protective OL at oxidation temperatures above 600 °C. Based on literature results, it is a well-known fact that the OL cracks and loses its cohesion with the metal at the metal/oxide interface when it reaches a critical thickness [8,9,48–50]. It seems this critical thickness was not reached for the oxidations performed at 500 and 538 °C studied here. According to literature, the delamination of the OL is thought to be induced by the presence of internal stresses due to the large molar volume difference between the metal and the oxide [68,69]. Stringer explained that nanometric pores form inside the OL during its growth. These pores become larger as the OL layer thickens and internal stresses induce the breakdown of the OL [9]. This phenomena is clearly depicted in Fig. 17 with the delamination appearing where pores weaken the integrity of the OL.

Table 6 presents the ratio of ODZ thickness to OL thickness for samples oxidized 500 h at 600 °C and 2000 h at 500 °C. For both oxidation conditions, the ratio is similar for LBM P600 and EBM P600 samples, but it strongly depends on temperature. Indeed, after an oxidation of 500 h at 600 °C, ODZ thickness is about 3 times higher than OL thickness, whereas after 2000 h of oxidation at 500 °C, ODZ thickness is about 50 times higher than OL thickness. For all samples, Table 6 also shows which proportion of the mass gain is due to the oxide growth and which is due to the oxygen dissolution in the metal. These proportions were calculated using two methods. The first one is based on the total mass gain and on OL thickness measures with the hypothesis of a fully dense oxide. The second method consists in integrating EPMA concentration profiles with the hypothesis that the effect of volume expansion on alloy density, due to the oxygen ingress in the metal, is negligible. After 500 h of oxidation at 600 °C, the OL is thick and accounts for most of the mass gain (≈ 85 %). Whereas after 2000 h of oxidation at 500 °C, the OL is very thin and the mass gain is mainly due to the ODZ. At 500 °C, the oxide growth accounts for only 15 % of the mass gain, and most of the oxygen uptake is due to its dissolution into the metal.

Most of the oxidation studies on Ti-6Al-4V alloy reported in the literature were performed at temperatures above 600 °C, as seen in Fig. 6. The Ti-6Al-2Sn-4Zr-2Mo (Ti6242) alloy is a titanium near-α alloy used at temperatures up to 600 °C. Gaddam et al. studied both Ti-6Al-4V and Ti6242 alloys and observed that, at 593 °C, the latter alloy had much lower oxidation kinetics – in terms of mass gain – than the former [15]. For 200 h at 593 °C, Ti-6Al-4V had a mass gain of about 0.8 mg·cm^{-2} whereas Ti6242 had a mass gain of about 0.2 mg·cm^{-2}.

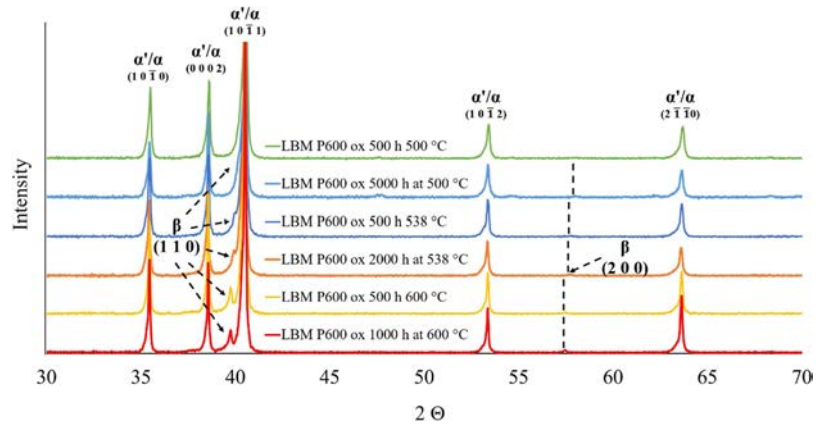

Fig. 15. XRD measurements of the bulk microstructure of LBM P600 samples after oxidation treatment.

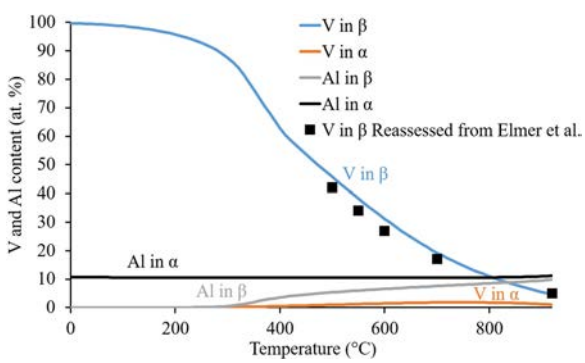

Fig. 16. V and Al content in α and β phases of Ti-6Al-4V calculated with TCTI 1 database in Thermo-Calc.

However, in their study Gaddam et al. also showed that for 500 h at 593 °C Ti6242 and Ti-6Al-4V alloys have the same "alpha-case" of 30 µm. It seems that, at 593 °C, the oxidation kinetics of Ti-6Al-4V is higher than the oxidation kinetics of Ti6242 only because the oxide scale grows faster. As mentioned previously, the higher OL thickness on Ti-6Al-4V at 593 °C is probably due to the presence of numerous defects in the oxide scale and to its delamination, which increases its formation rate. For oxidation tests carried out for 2000 h at 500 °C, the critical thickness was not reached and the formation rate of the OL is indeed relatively low, as shown by the thin OL thicknesses presented in Table 6. Moreover, by comparing EPMA-measured ODZ thickness of samples oxidized 2000 h at 500 °C in this study with the ODZ thickness, measured by optical microscopy and EPMA, of the Ti6242 alloy, with different oxygen concentration in the bulk, oxidized 500 h at 500 °C from Gaddam et al. [16], it can be seen that Ti-6Al-4V and Ti6242 alloys both have quite similar ODZ thicknesses.

4.4. ODZ and embrittlement

Fig. 13 shows that the rupture mode of Ti-6Al-4V changed from ductile to brittle due to the presence of oxygen. As seen in Fig. 11, for LBM P600 and EBM P600 oxidized 500 h at 600 °C, the oxygen concentration at 25 µm from the metal/oxide interface is much lower than 1 at.%. It can therefore be assumed that a small concentration of oxygen (< 1 at.% of oxygen) is enough to change the rupture mode. The quantification of the oxygen concentration responsible for the change in rupture mode cannot be determined precisely with EPMA. As explained previously, the machine error of EPMA measurement is about 0.3 wt.%, i.e. 0.9 at.%. Nevertheless, the modelled diffusion profile allows to estimate the oxygen concentration at a depth of 25 µm. This value is about 0.4 +/− 0.9 at.% taking into account the initial bulk oxygen concentration of 0.3 at.%. This value of "less than 1 at.%" is consistent with literature results [20,24]. In addition, Yan et al. used an atomic probe and found that an oxygen concentration of 0.33 wt.% (≈ 0.9 at.%) is enough to have a drastic drop in ductility and "reach total brittleness" in the Ti-6Al-4 alloy [70]. Similarly, Liu et al. confirmed that an oxygen concentration of about 0.65 wt.% induced a change in rupture mode from ductile to brittle for an α titanium alloy resulting in a rupture along α-lath boundaries and a cleavage through α-laths [53].

5. Conclusions

The main purpose of this study was to determine the influence of the specific surface state and microstructure of the Ti-6Al-4V alloy fabricated by Laser Beam Melting and Electron Beam Melting on high temperature oxidation, and to compare the behaviour of these materials with conventionally processed Ti-6Al-4V. The present study led to the following conclusions:

1) The surface of LBM and EBM Ti-6Al-4V alloys are rough. The presence of partially-melted powder grains increases the surface area

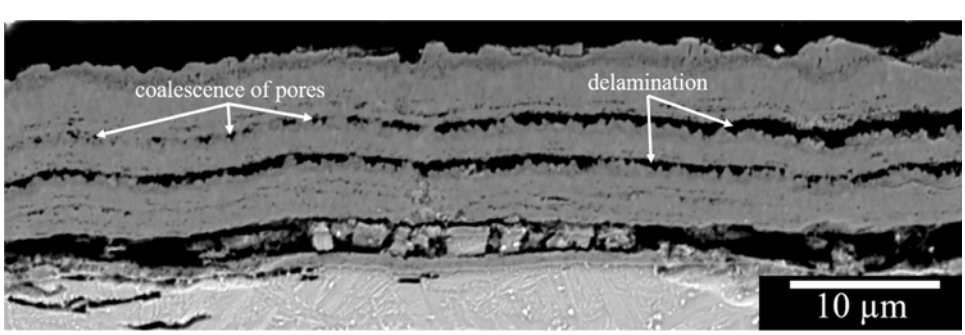

Fig. 17. Breakdown of OL of LBM P600 sample oxidized 1 000 h at 600 °C.

by a factor of 2–5. It was shown that the higher net mass change per unit area obtained for as-built samples in this study were only due to their higher surface area. As far as OL and ODZ thicknesses are concerned, the oxidation kinetics of as-built LBM and EBM are similar to ground LBM and EBM samples respectively, and they do not explain the differences in mass gains.

2) Oxidation kinetics of Ti-6Al-4V titanium alloys fabricated by LBM and EBM are similar to that of conventionally processed Ti-6Al-4V alloys at 600 °C, and to that of other conventional Ti-6Al-4V alloys reported in the literature. Oxidation treatments performed on HIP-treated EBM and EBM samples show that α-lath thickness and the number of α interfaces inside the metal does not have an influence on oxidation kinetics nor on oxygen diffusion in the metal. The oxidation of LBM samples shows that the α' microstructure is not stable during oxidation treatment at 500 and 600 °C and transforms into a (α + β) microstructure.
3) The oxide layer is mainly composed of rutile (TiO_2) with presence of alumina (Al_2O_3) when the oxidation is long enough. Results also show that there is a high density of pores inside the oxide layer and at the metal/oxide interface, and this porosity increases as oxidation progresses. These pores weaken the oxide layer which deteriorates due to the presence of internal stresses once a critical thickness is reached. At 600 °C, the oxide layer accounts for about 80 % of the oxygen intake, whereas at 500 °C less than 20 % of the oxygen is in the oxide scale. At 600 °C the critical oxide layer thickness is reached before a few dozen hours, whereas, at 500 °C, it still had not been reached after 5 000 h oxidation tests.
4) With the ingress of oxygen in the metal, the ductile rupture mode of the Ti-6Al-4V alloy fabricated by LBM and EBM switches to a brittle rupture mode. It was found that an oxygen concentration lower than 1 at.% was sufficient to embrittle the alloy.

Data availability

The raw/processed data required to reproduce these findings cannot be shared at this time as the data also forms part of an ongoing study.

Declaration of Competing Interest

The authors declare that they have no known competing financial interests or personal relationships that could have appeared to influence the work reported in this paper.

Acknowledgments

This work performed at CIRIMAT laboratory falls within the framework of the Andduro project hosted by the French Institute of Technology IRT Saint Exupery, supported by the Occitanie Region and industrial partners. The authors gratefully acknowledge Claudie Josse, Sophie Gouy (UMS Castaing, Toulouse, France) for their technical assistance on FIB cross-section observations and EPMA measurements respectively, Julien Milanese and Jean-Baptiste Osio (MIDIVAL, France) for their technical assistance on tensile tests and François Jomard (GeMac, UVSQ, Versailles, France) for SIMS measurements.

References

[1] R.R. Boyer, Titanium for aerospace: rationale and applications, Adv. Perform. Mater. 2 (4) (1995) 349–368.
[2] R.R. Boyer, An overview on the use of titanium in the aerospace industry, Mater. Sci. Eng. A-Struct. Mater. Proper. Microstruct. Process. 213 (1–2) (1996) 103–114.
[3] R.R. Boyer, Titanium airframe applications: brief history, present applications and future trends, Mater. Sci. Forum (2003) 426–432 pt.1.
[4] M. Peters, J. Kumpfert, C.H. Ward, C. Leyens, Titanium alloys for aerospace applications, Adv. Eng. Mater. 5 (6) (2003) 419–427.
[5] L. Badea, M. Surand, J. Ruau, B. Viguier, Creep behavior of Ti-6Al-4V from 450°C to 600°C, Univ. Polytech. Bucharest Sci. Bull. Ser. B 76 (1) (2014) 185–196.
[6] E. Gemelli, N.H.A. Camargo, Oxidation kinetics of commercially pure titanium, Revista Matéria 12 (3) (2007) 525–531.
[7] B. Champin, L. Graff, M. Armand, G. Béranger, C. Coddet, Oxydation des alliages de titane au voisinage des températures d'utilisation dans les turbomoteurs, J. Less Common Met. 69 (1980) 163–183.
[8] H.L. Du, P.K. Datta, D.B. Lewis, J.S. Burnellgray, Air oxidation behavior of Ti-6al-4v alloy between 650-degrees-C and 850-degrees-C, Corros. Sci. 36 (4) (1994) 631–642.
[9] J. Stringer, The oxidation of titanium in oxygen at high temperatures, Acta Metall. 8 (1960) 758–766.
[10] P. Kofstad, P.B. Anderson, O.J. Krudtaa, Oxidation of titanium in the temperature range 800–1200°C, J. Less-Common Met. 3 (1961) 89–97.
[11] P. Kofstad, High Temperature Oxidation of Metals, Wiley, New York, 1966.
[12] A.M. Chaze, C. Coddet, Influence of aluminium on the oxidation of titanium between 550 and 750°C, J. Less-Common Met. 157 (1990) 55–70.
[13] S. Frangini, A. Mignone, F. de Riccardis, Various aspects of the air oxidation behaviour of a Ti6Al4V alloy at temperatures in the range 600–700 °C, J. Mater. Sci. 29 (3) (1994) 714–720.
[14] H. Güleryüz, H. Çimenoğlu, Effect of thermal oxidation on corrosion and corrosion–wear behaviour of a Ti–6Al–4V alloy, Biomaterials 25 (16) (2004) 3325–3333.
[15] R. Gaddam, B. Sefer, R. Pederson, M.L. Antti, Study of alpha-case depth in Ti-6Al-2Sn-4Zr-2Mo and Ti-6Al-4V, IOP Conf. Ser.: Mater. Sci. Eng. 48 (1) (2013) 012002.
[16] R. Gaddam, M.L. Antti, R. Pederson, Influence of alpha-case layer on the low cycle fatigue properties of Ti-6Al-2Sn-4Zr-2Mo alloy, Mater. Sci. Eng. A 599 (Supplement C) (2014) 51–56.
[17] D.A. Brice, P. Samimi, I. Ghamarian, Y. Liu, R.M. Brice, R.F. Reidy, J.D. Cotton, M.J. Kaufman, P.C. Collins, Oxidation behavior and microstructural decomposition of Ti-6Al-4V and Ti-6Al-4V-1B sheet, Corros. Sci. 112 (2016) 338–346.
[18] L. Li, K. Yu, K. Zhang, Y. Liu, Study of Ti–6Al–4V alloy spectral emissivity characteristics during thermal oxidation process, Int. J. Heat Mass Transf. 101 (2016) 699–706.
[19] K. Maeda, S. Suzuki, K. Ueda, T. Kitashima, S.K. Bhattacharya, R. Sahara, T. Narushima, Experimental and theoretical study of the effect of Si on the oxidative behavior of Ti-6Al-4V alloys, J. Alloys. Compd. 776 (2019) 519–528.
[20] W.L. Finlay, J.A. Snyder, Effects of three interstitial solutes (Nitrogen, Oxygen and Carbon) on the mechanical properties of high-purity alpha titanium, J. Met. 188 (1950) 227–286.
[21] P. Kofstad, K. Hauffe, H. Kjollesdal, Investigation on the oxidation mechanism of titanium, Acta Chem. Scand. 12 (1958) 239–266.
[22] C.E. Shamblen, T.K. Redden, R.I. Jaffee (Ed.), Air Contamination and Embrittlement of Titanium Alloys, Science, Technology, and Application of Titanium, Oxford Pergamon Press Ltd., 1970, pp. 199–208 1970.
[23] L. Bendersky, A. Rosen, The effect of exposure on fracture of Ti-6AL-4V alloy, Eng. Fract. Mech. 13 (1) (1984) 111–118.
[24] R.N. Shenoy, J. Unnam, R.K. Clark, Oxidation and embrittlement of Ti-6Al-2Sn-4Zr-2Mo alloy, Oxid. Met. 26 (1–2) (1986) 105–124.
[25] H. Fukai, H. Iizumi, K. Minakawa, C. Ouchi, The effects of the oxygen-enriched surface layer on mechanical properties of alpha + beta type titanium alloys, Isij Int. 45 (1) (2005) 133–141.
[26] K. Kakehi, T. Hashimoto, Influence of oxidation on mechanical properties of the heat-resistant titanium alloy DAT54, J. Jpn. Inst. Met. 72 (10) (2008) 819–824.
[27] G. Lütjering, J.C. Williams, Titanium, (2007).
[28] S.L. Sing, J. An, W.Y. Yeong, F.E. Wiria, Laser and electron-beam powder-bed additive manufacturing of metallic implants: a review on processes, materials and designs, J. Orthop. Res. 34 (3) (2016) 369–385.
[29] J.J. Beaman, H.L. Marcus, D.L. Bourell, J.W. Barlow, R.H. Crawford, K.P. McAlea, Solid Freeform Fabrication: A New Direction in Manufacturing, Kluwer Academic Publishers, 1997.
[30] S.S. Al-Bermani, M.L. Blackmore, W. Zhang, I. Todd, The origin of microstructural diversity, texture, and mechanical properties in electron beam melted Ti-6Al-4V, Metall. Mater. Trans. A 41 (13) (2010) 3422–3434.
[31] L.E. Murr, S.A. Quinones, S.M. Gaytan, M.I. Lopez, A. Rodela, E.Y. Martinez, D.H. Hernandez, E. Martinez, F. Medina, R.B. Wicker, Microstructure and mechanical behavior of Ti–6Al–4V produced by rapid-layer manufacturing, for biomedical applications, J. Mech. Behav. Biomed. Mater. 2 (1) (2009) 20–32.
[32] M. Simonelli, Y.Y. Tse, C. Tuck, Further Understanding of Ti-6Al-4V Selective Laser Melting Using Texture Analysis, (2012), pp. 1–4.
[33] M. Koike, K. Martinez, L. Guo, G. Chahine, R. Kovacevic, T. Okabe, Evaluation of titanium alloy fabricated using electron beam melting system for dental applications, J. Mater. Process. Technol. 211 (8) (2011) 1400–1408.
[34] L.E. Murr, E. Martinez, K.N. Amato, S.M. Gaytan, J. Hernandez, D.A. Ramirez, P.W. Shindo, F. Medina, R.B. Wicker, Fabrication of metal and alloy components by additive manufacturing: examples of 3D materials science, J. Mater. Res. Technol. 1 (1) (2012) 42–54.
[35] T. Scharowsky, V. Juechter, R.F. Singer, C. Körner, Influence of the scanning strategy on the microstructure and mechanical properties in selective Electron beam melting of Ti–6Al–4V, Adv. Eng. Mater. 17 (11) (2015) 1573–1578.
[36] C. Qiu, N.J.E. Adkins, M.M. Attallah, Microstructure and tensile properties of selectively laser-melted and of HIPed laser-melted Ti–6Al–4V, Mater. Sci. Eng. A 578 (2013) 230–239.
[37] J. Karlsson, M. Norell, U. Ackelid, H. Engqvist, J. Lausmaa, Surface oxidation behavior of Ti–6Al–4V manufactured by electron beam melting (EBM®), J. Manuf. Process. 17 (Supplement C) (2015) 120–126.
[38] M.J. Bermingham, J. Thomson-Larkins, D.H. St John, M.S. Dargusch, Sensitivity of Ti-6Al-4V components to oxidation during out of chamber Wire + Arc Additive Manufacturing, J. Mater. Process. Technol. 258 (2018) 29–37.
[39] J.D.A. Caballero, Y. Bandari, S. Williams, Oxidation of Ti-6Al-4V during wire and

arc additive manufacture, 3D Print. Addit. Manuf. 6 (2) (2019) 91–98.
[40] M. Terner, S. Biamino, G. Baudana, A. Penna, P. Fino, M. Pavese, D. Ugues, C. Badini, Initial oxidation behavior in air of TiAl-2Nb and TiAl-8Nb alloys produced by electron beam melting, J. Mater. Eng. Perform. 24 (10) (2015) 3982–3988.
[41] I. Som, V.K. Balla, M. Das, D. Sukul, Thermally oxidized electron beam melted γ-TiAl: in vitro wear, corrosion, and biocompatibility properties, J. Mater. Res. 33 (14) (2018) 2096–2105.
[42] J. Wang, Z. Pan, Y. Ma, Y. Lu, C. Shen, D. Cuiuri, H. Li, Characterization of wire arc additively manufactured titanium aluminide functionally graded material: microstructure, mechanical properties and oxidation behaviour, Mater. Sci. Eng. A 734 (2018) 110–119.
[43] Y. Zhou, S.F. Wen, B. Song, X. Zhou, Q. Teng, Q.S. Wei, Y.S. Shi, A novel titanium alloy manufactured by selective laser melting: microstructure, high temperature oxidation resistance, Mater. Des. 89 (2016) 1199–1204.
[44] Z. Liang, B. Tang, Y. Gui, Q. Zhao, High-temperature oxidation behavior of the Ti-6Al-4V alloy manufactured by selective laser sintering, JOM 71 (10) (2019) 3600–3605.
[45] T. Sanviemvongsak, D. Monceau, B. Macquaire, High temperature oxidation of IN 718 manufactured by laser beam melting and electron beam melting: effect of surface topography, Corros. Sci. 141 (2018) 127–145.
[46] A. Casadebaigt, J. Hugues, D. Monceau, Influence of microstructure and surface roughness on oxidation kinetics at 500–600 °C of Ti–6Al–4V alloy fabricated by additive manufacturing, Oxid. Met. 90 (5) (2018) 633–648.
[47] V. Juechter, T. Scharowsky, R.F. Singer, C. Körner, Processing window and evaporation phenomena for Ti–6Al–4V produced by selective electron beam melting, Acta Mater. 76 (Supplement C) (2014) 252–258.
[48] P. Sarrazin, C. Coddet, Oxidation of titanium-alloy Ta6v4 by dry oxygen between 700 degrees centigrade and 1000 degrees centigrade. 1. Experimental results, Corros. Sci. 14 (1) (1974) 83–89.
[49] F. Motte, C. Coddet, P. Sarrazin, M. Azzopardi, J. Besson, Comparative-study of oxidation with water-vapor of pure titanium and of Ti-6al-4v, Oxid. Met. 10 (2) (1976) 113–126.
[50] C. Coddet, P. Sarrazin, J. Besson, Essai d'interprétation du mécanisme d'oxydation de l'alliage de titane TA6V4 par l'oxygène sec entre 700 °C et 1000 °C, J. Less Common Met. 51 (1) (1977) 1–12.
[51] E. Dong, W. Yu, Q. Cai, L. Cheng, J. Shi, High-temperature oxidation kinetics and behavior of Ti–6Al–4V alloy, Oxid. Met. 88 (5) (2017) 719–732.
[52] N. Vaché, D. Monceau, Oxygen diffusion modeling in titanium alloys: new elements on the analysis of microhardness profiles, Oxid. Met. 93 (1) (2020) 215–227.
[53] Z. Liu, G. Welsch, Literature survey on diffusivities of oxygen, aluminium and vanadium in Alpha Titanium, Beta titanium and in rutile, Metall. Trans. 19A (04) (1988) 1121–1125.
[54] R.I.J.H.R. Ogden, The Effects of Carbon, Oxygen, and Nitrogen on the Mechanial Properties of Titanium and Titanium Alloys, TML Report n°20 (1955).
[55] J. Han, J. Yang, H. Yu, J. Yin, M. Gao, Z. Wang, X. Zeng, Microstructure and mechanical property of selective laser melted Ti6Al4V dependence on laser energy density, Rapid Prototyp. J. 23 (2) (2017) 217–226.
[56] D. Buchbinder, H. Schleifenbaum, S. Heidrich, W. Meiners, J. Bültmann, High power selective laser melting (HP SLM) of aluminum parts, Phys. Procedia 12 (2011) 271–278.
[57] Y. Combres, Traitements thermiques des alliages de titane, Techniques de l'ingénieur M1335, (2013).
[58] L.Y. Chen, J.C. Huang, C.H. Lin, C.T. Pan, S.Y. Chen, T.L. Yang, D.Y. Lin, H.K. Lin, J.S.C. Jang, Anisotropic response of Ti-6Al-4V alloy fabricated by 3D printing selective laser melting, Mater. Sci. Eng. A 682 (2017) 389–395.
[59] B. Vrancken, Study of Residual Stresses in Selective Laser Melting, KU Leuven - Faculty of Engineering Science, 2016.
[60] M.G. Ter Haar, H.T. Becker, Selective laser melting produced Ti-6Al-4V: post-process heat treatments to achieve superior tensile properties, Materials 11 (1) (2018).
[61] J. Yang, H. Yu, J. Yin, M. Gao, Z. Wang, X. Zeng, Formation and control of martensite in Ti-6Al-4V alloy produced by selective laser melting, Mater. Des. 108 (2016) 308–318.
[62] W. Xu, M. Brandt, S. Sun, J. Elambasseril, Q. Liu, K. Latham, K. Xia, M. Qian, Additive manufacturing of strong and ductile Ti–6Al–4V by selective laser melting via in situ martensite decomposition, Acta Mater. 85 (2015) 74–84.
[63] J.W. Elmer, T.A. Palmer, S.S. Babu, E.D. Specht, In situ observations of lattice expansion and transformation rates of α and β phases in Ti–6Al–4V, Mater. Sci. Eng. A 391 (1) (2005) 104–113.
[64] P. Pietrokowsky, P. Duwez, Partial titanium-vanadium phase diagram, JOM 4 (6) (1952) 627–630.
[65] T. Sugahara, D.A.P. Reis, C. Moura Neto, M.J.R. Barboza, E.A.C. Perez, F. Piorino Neto, A.C.O. Hirschmann, The effect of Widmanstatten and equiaxed microstructures of Ti-6Al-4V on the oxidation rate and creep behavior, Adv. Mater. Forum (2010) 657–662 Pt 1 and 22010.
[66] C. Leyens, M. Peters, W.A. Kaysser, Influence of microstructure on oxidation behaviour of near-alpha titanium alloys, Mater. Sci. Technol. 12 (3) (1996) 213–218.
[67] K.V. Sai Srinadh, V. Singh, Oxidation behaviour of the near alpha-titanium alloy IMI 834, Bull. Mater. Sci. 27 (4) (2004) 347–354.
[68] J. Stringer, Stress generation and relief in growing oxide films, Corros. Sci. 10 (1970) 513–543.
[69] J. Philibert, L'oxydation à chaud des métaux, La revue de métallurgie-CIT/Science et génie des matériaux, (1993).
[70] M. Yan, M.S. Dargusch, T. Ebel, M. Qian, A transmission electron microscopy and three-dimensional atom probe study of the oxygen-induced fine microstructural features in as-sintered Ti–6Al–4V and their impacts on ductility, Acta Mater. 68 (2014) 196–206.
[71] H. Guleryuz, H. Cimenoglu, Oxidation of Ti-6Al-4V alloy, J. Alloys. Compd. 472 (1–2) (2009) 241–246.
[72] D. Poquillon, C. Armand, J. Huez, Oxidation and oxygen diffusion in Ti–6al–4V alloy: improving measurements during sims analysis by rotating the sample, Oxid. Met. 79 (3–4) (2013) 249–259.
[73] J.H. Luan, Z.B. Jiao, G. Chen, C.T. Liu, Improved ductility and oxidation resistance of cast Ti–6Al–4V alloys by microalloying, J. Alloys. Compd. 602 (2014) 235–240.
[74] C. Ciszak, I. Popa, J.-M. Brossard, D. Monceau, S. Chevalier, NaCl induced corrosion of Ti-6Al-4V alloy at high temperature, Corros. Sci. 110 (2016) 91–104.
[75] G. Fargas, J.J. Roa, B. Sefer, R. Pederson, M.L. Antti, A. Mateo, Oxidation behavior of TI-6Al-4V alloy exposed to isothermal and cyclic thermal treatments, 26th International Conference on Metallurgy and Materials METAL 2017, Brno, Czech Republic, May 24th–26th, 2017, TANGER Ltd., 2017, pp. 1573–1579.
[76] S.A. Tsipas, E. Gordo, A. Jiménez-Morales, Oxidation and corrosion protection by halide treatment of powder metallurgy Ti and Ti6Al4V alloy, Corros. Sci. 88 (2014) 263–274.
[77] F. Borgioli, E. Galvanetto, F. Iozzelli, G. Pradelli, Improvement of wear resistance of Ti–6Al–4V alloy by means of thermal oxidation, Mater. Lett. 59 (17) (2005) 2159–2162.
[78] P.A. Dearnley, K.L. Dahm, H. Çimenoğlu, The corrosion–wear behaviour of thermally oxidised CP-Ti and Ti–6Al–4V, Wear 256 (5) (2004) 469–479.
[79] H. Guleryuz, H. Cimenoglu, Surface modification of a Ti–6Al–4V alloy by thermal oxidation, Surf. Coat. Technol. 192 (2) (2005) 164–170.
[80] S. Kumar, T.S.N. Sankara Narayanan, S. Ganesh Sundara Raman, S.K. Seshadri, Thermal oxidation of Ti6Al4V alloy: microstructural and electrochemical characterization, Mater. Chem. Phys. 119 (1–2) (2010) 337–346.